21st Australasian Fluid Mechanics Conference
Adelaide, Australia
10-13 December 2018

Vortex Rings Ejected From Flush-mounted and Elevated Pipes

E. R. Hassan and R. M. Kelso

School of Mechanical Engineering
University of Adelaide, Adelaide, South Australia 5005, Australia

Abstract

This paper describes observations and measurements of the effects of a change in boundary conditions on the vorticity field and circulation of laminar vortex rings ejected from a circular pipe. The change in boundary conditions is from a pipe exit which is flush with a flat wall, to a pipe exit which is elevated above the wall. Measurements of the evolving vorticity field show that the flush-mounted vortex ring has a smaller ring diameter than the elevated vortex ring. This is the result of the vortex rings interaction with the wall, which is equivalent to the influence of an imaginary image vortex ring below the wall (i.e. the method of images). The image induces a radially-inward motion towards the axis of the pipe. Plotting vortex ring circulation as a function of time shows that both vortex rings have the same maximum circulation, but the rate of circulation decay is greater in the flush-mounted vortex ring. This is explained in terms of increased rate of cancellation of opposite-sign vorticity at the vortex ring centre.

Introduction

Vortex rings have been studied for over 100 years. Vortex rings can be formed be impulsively ejecting fluid from a pipe for a short duration of time. Lim and Nickels [6] show that features of vortex rings are affected by the geometry of the pipe used to generate them.

In this study we investigate the generation and subsequent development of a single vortex ring generated with two distinct boundary conditions. The change in boundary condition is from a pipe exit which is flush with a flat wall, to a pipe exit which is elevated above the wall. From velocity measurements in the plane containing the axis of the vortex ring we obtain the vorticity and the circulation of principal structures in the developing flow field.

Apparatus

Experiments are conducted in a confined section of a closed-return water channel with a working section of 500 mm $\times$ 500 mm $\times$ 2000 mm. A vortex ring is generated by impulsively translating a piston within a cylinder for a short period with the ideal piston velocity having a square-wave function of time. A stepper motor driving a lead screw advances the piston in a controlled and repeatable manner.

Fluid from the cylinder flows through a hose into a pipe of diameter D=25 mm. Two pipe geometries are considered. In the "flush-mounted" geometry, the exit plane of the pipe is flush mounted with the floor of the of the working section of the water channel. In the "elevated" gemoetry, the pipe exit plane is 2.5D above the floor of the water channel and the outside of the pipe is tapered at an angle of 7^o to a sharp edge at the tip. These geometries and related coordinate systems are shown schematically in figure 1.

PIV Method

Velocity components in the plane containing the axis of the pipe

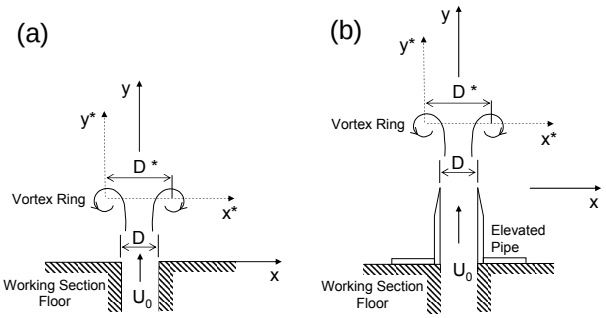

Figure 1: Configurations and coordinate systems of the (a) flush-mounted and (b) elevated geometries

	Flush-mounted	Elevated
PIV image size (mm $\times$ mm)	126 $\times$ 126	93 $\times$ 93
Spatial resolution (px/mm)	8.00	10.85
Number of realisations	35	47

Table 1: Experimental parameters.

are measured by two-component Particle Image Velocimetry (2C-PIV). The flow is seeded with 8 μm mean-diameter hollow glass spheres of a specific gravity 1.1. Illumination is provided by a dual-cavity Quantel Brilliant B Nd:YAG laser. The wavelength of the laser light is 532 nm and the duration of each laser pulse is approximately 5 ns. From the laser beam, an optics train generates a light sheet of thickness 1.5 mm. The PIV images are recorded by a Kodak Megaplus ES 1.0 CCD camera with an array of 1008 pixels $\times$ 1018 pixels and a Nikon 70-300 mm zoom lens. PIV image pairs are collected at a rate of 10 Hz with a time delay of 10 ms between the laser pulses illuminating the first and second images in each pair. A Stanford DG535 pulse-delay generator regulates the triggering of the laser pulses from each laser cavity. XCAP-Plus software collects and transfers images to computer hard disk as uncompressed 16-bit TIFF files. PIV velocity vectors are obtained by cross correlation of the image pairs. An interrogation-window size of 32 pixels $\times$ 32 pixels is used with 50 % overlap. Correlation peaks are detected using a multi-pass double correlation, least squares Gaussian fit. Anomalous velocity vectors (outliers) are detected using a custom-built code which implements the universal median technique described by Westerweel and Scarano [9]. Detected outliers are replaced with a weighted average of valid surrounding vectors. For all results presented here, the number of outliers in any one velocity-vector field is less than 3% of the total number of vectors. An adaptive Gaussian window interpolator filters noise from the raw vector field. The flush and elevated cases were conducted at different times during a larger experimental campaign. As a result, there are differences in the sizes of PIV image region and resulting spatial resolution. Table 1 shows the size of the PIV image region, resulting spatial resolution, the number of times each flow was

repeated for each of the geometric configurations. The velocity uncertainty, $(\delta_u/u_0)_{\max}$, is 11.5% and 8.1% for the flush and elevated cases respectively. This velocity uncertainty is evaluated for the worst-case conditions where the velocity gradient is largest. Elsewhere the error is significantly smaller.

A custom-built electronic controller synchronises the start of vortex generation with the next available laser pulse and enables the camera trigger. This ensures that the n-th PIV image pair in any one realisation is synchronised with the n-th image pair in all other realisations.

Flow Conditions

The flow conditions for flush and elevated vortex rings are identical. The vortex rings are generated by impulsively translating the piston within a cylinder for a duration of τ = 1 second. The spatially-averaged pipe exit velocity, $\overline{U(t)}$, is integrated over time to obtain the total length of the displaced fluid slug, $L_0 = \int_0^\infty \overline{U(t)}dt \approx 40$mm. Figure 2 shows the instantaneous spatially-averaged pipe exit velocity $\overline{U(t)}$, and displaced slug length $L(t) = \int_0^t \overline{U(t)}dt$. The ratio of the displaced slug length to the duration of piston motion, $U_0 = L_0/\tau \approx 40$mm/s, is a vortex ring velocity scale. The period of piston motion corresponds to a nondimensional time of $\widetilde{t} = tU_0/D = 1.6$. The Reynolds number of the vortex ring can be defined in terms of the circulation of the vortex ring, $Re_\Gamma = \Gamma/\nu$. The vortex slug model described by Shariff and Leonard [8] provides a convenient estimate of the circulation, Γ_{slug} such that

$$Re_\Gamma = \frac{\Gamma_{slug}}{\nu} \approx \frac{\frac{1}{2}U_0^2\tau}{\nu}. \quad (1)$$

For the current data $Re_\Gamma \approx 800$ and the relative length of the extruded fluid slug is L/D ≈ 1.6. The latter value is below the critical value of L/D ≈ 4 above which the vortex ring is followed by a trailing jet as described by Gharib *et al* [4]

Data Processing

The out-of-plane vorticity field, ω_z, of each time step of each realisation is estimated from the in-plane velocity components. The hybrid compact-Richardson extrapolation (CR4) vorticity-estimation scheme of Etebari & Vlachos [2] is a noise-optimised, fourth-order scheme which simultaneously reduces both the random error and the bias error. This vorticity estimation scheme is applied to all the data. The error propagation analysis of Fouras & Soria [3] is used to estimate the maximum random and bias errors in the vorticity estimate. The total vorticity uncertainty, $(\delta_\omega/\omega_0)|_{\max}$, is 12.7% and 9.4% for the flush and elevated cases respectively. Vorticity is presented in the nondimensional form, $\widetilde{\omega}=\omega_z D/U_0$.

Circulation, Γ, of each vortex core is estimated by numerically integrating velocity components around the boundary of a region in which vorticity exceeds a threshold value. For this investigation, the threshold level is $\widetilde{\omega}$=0.4, which corresponds to approximately 4% of the peak vorticity. Details of the method and the associated error analysis are given in Hassan *et al.* [5]. The total circulation uncertainty, $(\delta_\Gamma/\Gamma_0)|_{\max}$, is 5.4% and 4.6% for the flush and elevated cases respectively. Circulation is presented in the nondimensional form, $\widetilde{\Gamma}=\Gamma/(U_0D)$.

Vorticity and circulation are estimated for each realisation and at each time step.

Evolution of the vortex ring

For both geometries, the vortex ring forms as the piston pushes fluid from the pipe, and the vortex ring moves away along the axis of symmetry of the pipe. Figure 3 shows the nondimensional vorticity field of the vortex ring at a nondimensional time of $\widetilde{t} = 4$ after the start of piston motion. Two cross-sections of the vortex ring are visible in the figure for each geometry. The cross-section on the left has positive vorticity and, for convenience, is referred to as the positive core. The cross-section on the right has negative vorticity and is referred to as the negative core. Also for convenience, we define the centre of each vortex core as the location of the local maximum of absolute vorticity. The cores initially grow in time but remain approximately equal in size and they remain symmetrically disposed about the axis of the pipe. Remnants of the stopping vortex, which is generated by cessation of piston motion, are visible at the pipe exit.

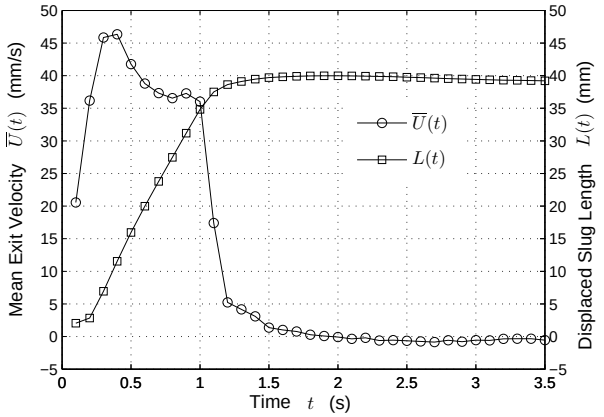

Figure 2: Average exit velocity $\overline{U(t)}$, and displaced slug length $L(t)$ verses time for a pulse duration of τ = 1 s.

To measure the distance between the vortex cores and to plot the distribution of vorticity between them, we map the vorticity-field data onto a new coordinate system (x^*, y^*) which moves with the vortex cores. The origin (x^*, y^*)=$(0,0)$ is at the centre of the positive core and the x^* axis joins the centres of the vortex cores as shown in figure 1. The mapping is performed at every time step and for every realisation. At each time step the vorticity distribution along the x^* axis is ensemble averaged over all the realisations and is plotted in figure 4 as a function of time.

The distance between vortex centres, which is a characteristic diameter D^* of the vortex ring, is shown in figure 4 as sequences of white dots. For both geometries, the vortex-ring diameter, D^* increases steadily up to a maximum until $\widetilde{t}$=1.6 when the piston stops. The diameter then decreases sharply, then grows slowly with time thereafter. At every time step, the diameter of the flush vortex ring is smaller than that of the elevated one. This is the result of the vortex ring's interaction with the wall, which is equivalent to the influence of an imaginary image vortex ring below the wall (i.e. the method of images). The image induces a radially-inward motion towards the axis of the pipe.

After $\widetilde{t} = 2$ the vorticity distribution between the cores remains almost anti-symmetric about the midpoint between vortex cores. Figure 5 shows the dimensionless ensemble-averaged vorticity distribution across the vortex cores at a nondimensional time of $\widetilde{t} = 6.7$. Soon after vortex formation, the vorticity profiles across each core display a Gaussian-like distribution. As time increases, cancellation of opposite-sign vorticity occurs at the ring centre, causing the profiles to become distorted from the Gaussian profile.

Circulation growth and decay

The temporal development of the ensemble-averaged circula-

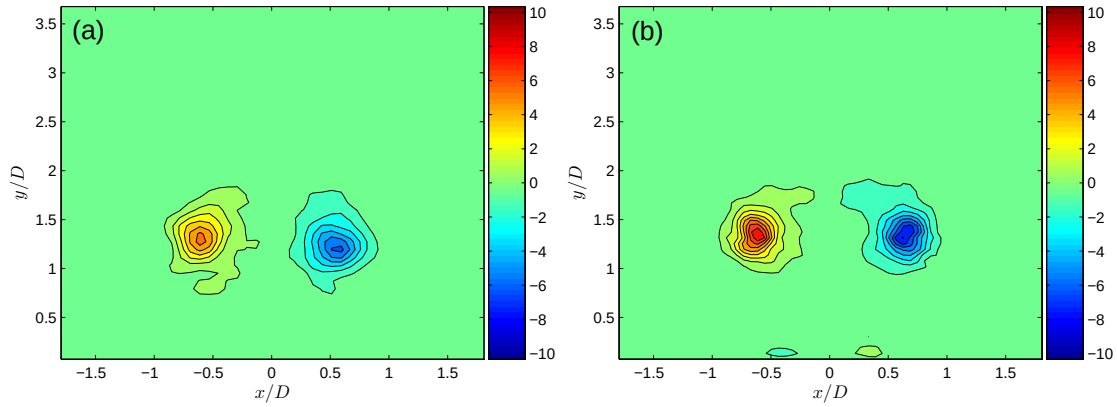

Figure 3: Nondimensional vorticity field, $\widetilde{\omega}$ of a vortex ring generated from a (a) flush-mounted and (b) elevated pipe at a nondimensional time of $\widetilde{t} = 4$.

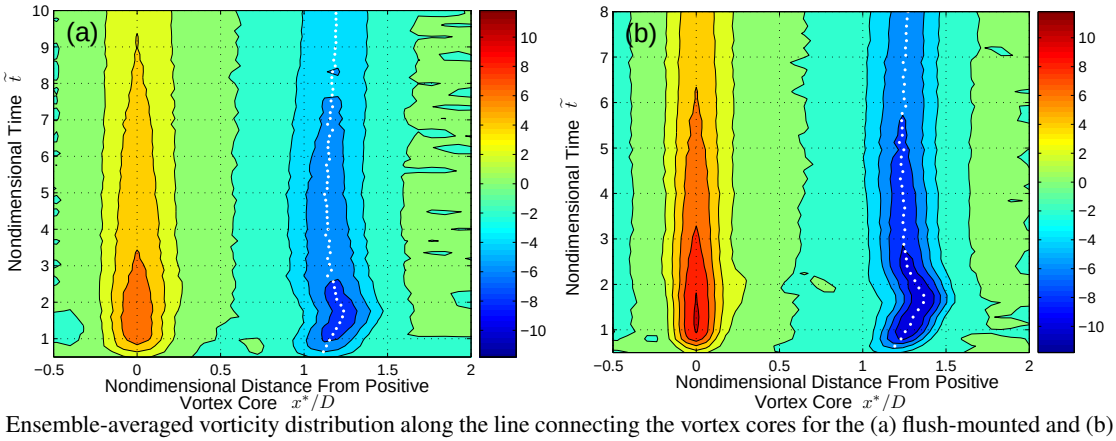

Figure 4: Ensemble-averaged vorticity distribution along the line connecting the vortex cores for the (a) flush-mounted and (b) elevated vortex rings. Maximum vorticity is at $x^*/D = 0$. The distance between vortex centres is shown as a sequence of white dots.

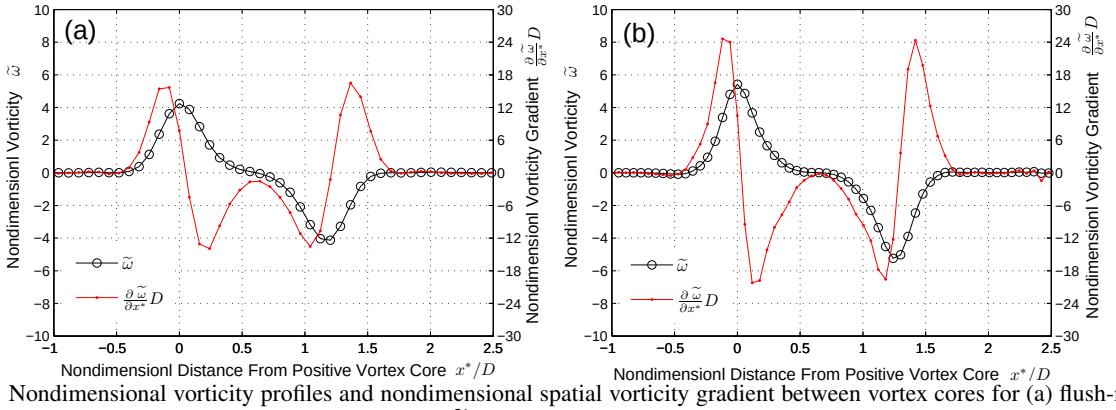

Figure 5: Nondimensional vorticity profiles and nondimensional spatial vorticity gradient between vortex cores for (a) flush-mounted and (b) elevated vortex ring at a nondimensional time of $\widetilde{t} = 6.7$.

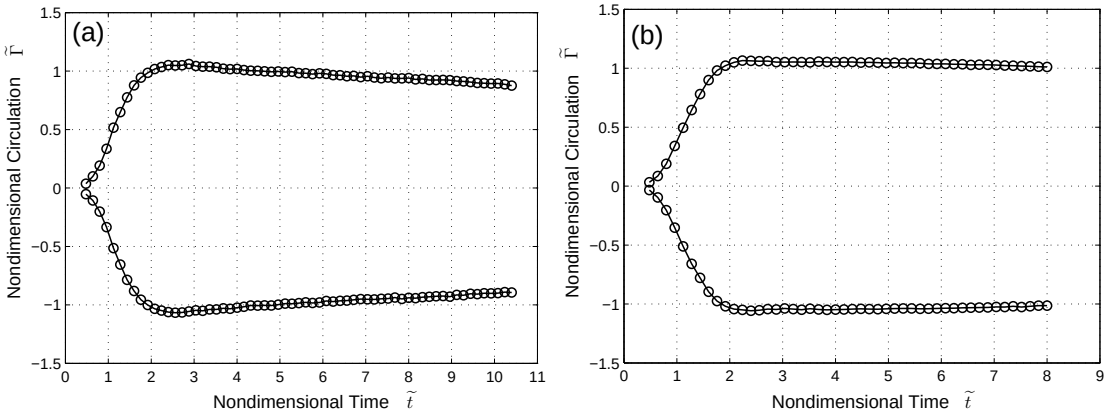

Figure 6: Growth and decay of ensemble-averaged nondimensional circulation of (a) flush-mounted and (b) elevated vortex rings.

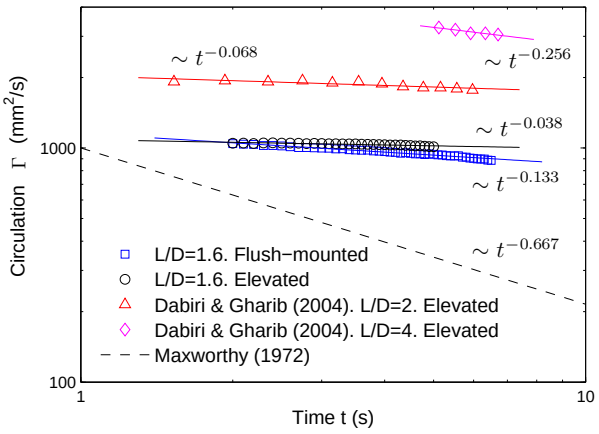

Figure 7: Decay of ensembled-averaged circulation for flush-mounted and elevated vortex rings compared with experimental data from Dabiri and Gharib [1] and the circulation decay model of Maxworthy [7]

tion of each vortex core is shown in figure 6. Positive values of circulation are measured for the positive cores and negative values for the negative cores. During the period of piston motion, $0 \lesssim \widetilde{t} \lesssim 1.6$, the magnitudes of circulation for both cores increase almost linearly with time. The rate of circulation growth is the same for the flush and elevated cases, and they reach their maximua a short time after the piston stops. The magnitudes of the peak circulations for flush and elevated cases are within 1.5% of each other, with that of the elevated case being slightly larger.

The circulation magnitude of each core then decays steadily with time. Figure 6 shows that the circulation values for the flush vortex ring cores decay faster than those of the elevated ones. Dabiri and Gharib [1] measure the circulation of vortex rings with stroke ratios of $L/D = 2$ and $L/D = 4$. Their data is compared to that from the current study in figure 7. Decay rates are obtained by fitting straight lines to the data. The analytic model of Maxworthy [7] is shown for reference. It is clear from the figure that the circulation decay rate of the flush vortex rings is greater than that of the elevated rings in the present experiments.

Vortex-ring circulation can decay by the cancellation of positive and negative vorticity at the centre of the vortex ring. The increased rate of circulation decay in the flush-mounted vortex ring case can be attributed to a larger rate of vorticity cancellation. Compared to the elevated vortex ring, the flush-mounted vortex ring has a smaller diameter, which causes positive and negative cores to be closer to each other and more interaction of vorticity of opposite-sign at the ring centre, hence a larger rate of vorticity cancellation.

The rate of vorticity cancellation at the vortex centre can be quantified by the magnitude of the spatial vorticity gradient, $\frac{\partial \omega}{\partial x}$ at the ring centre. Figure 5 shows the nondimensional spatial vorticity gradient for the flush-mounted and elevated vortex rings at a nondimensional time of $\widetilde{t} = 6.7$. The magnitude of the vorticity gradient is larger for the flush-mounted vortex ring at the vortex centre. The development of the vorticity gradient magnitude at the ring centre, $\left|\frac{\partial \widetilde{\omega}}{\partial x^*} D\right|_{x^*=D^*/2}$, with nondimensional time is shown if figure 8. After $\widetilde{t} \approx 3$ the vorticity gradient magnitude of the flush-mounted vortex ring is between two and seven that of the elevated ring. This increased rate of vorticity cancellation in the flush-mounted vortex ring is the cause of the increased circulation decay.

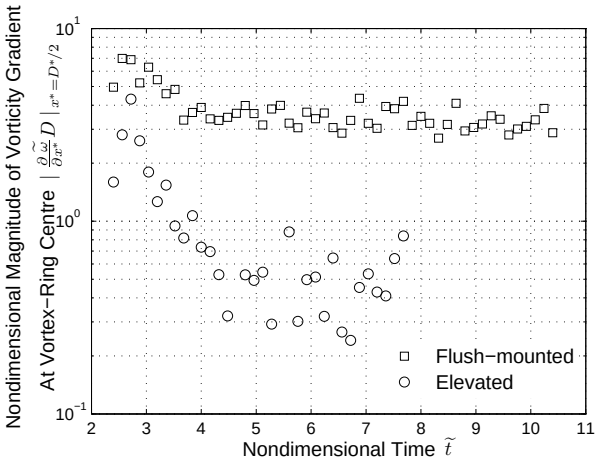

Figure 8: Temporal development of the spatial vorticity gradient magnitude for the flush mounted and elevated vortex rings.

Conclusions

Measurements of flow features of laminar flush-mounted and elevated vortex ring are made. It is observed that:

1. The diameters of vortex rings generated from the flush geometry are smaller than those generated from the elevated geometry under the same conditions.
2. The circulation growth rates of the vortex cores are the same for both geometries.
3. The circulation decay rates of flush vortex ring cores are greater than those of the elevated ones. This due to increased rate of cancellation of opposite-sign vorticity at the ring centre. This cancellation is characterised by the magnitude of the spatial vorticity gradient at the ring centre.

References

[1] Dabiri, J. and Gharib, M., Fluid entrainment by an isolated vortex ring, *Journal of Fluid Mechanics*, **511**, 2004, 311–331.

[2] Etebari, A. and Vlachos, P., Improvements on the accuracy of dervative estimation from dpiv velocity measurments., *Experiments in Fluids*, **39**, 2005, 1040–1050.

[3] Fouras, A. and Soria, J., Accuracy of out-of-plane vorticity measurements derived from in-plane velocity field data, *Experiments in Fluids*, **25**, 1998, 409–430.

[4] Gharib, M., Rambod, E. and Shariff, K., A universal time scale for vortex ring formation., *Journal of Fluid Mechanics*, **360**, 1998, 121–140.

[5] Hassan, E., Lau, T. and Kelso, R., Accuracy of circulation estimation schemes applied to discretised velocity field data, in *Proceedings of the Sixteenth Australasian Fluid Mechanics Conference, Gold Coast, Australia*, The University of Queensland, 2007.

[6] Lim, T. and Nickels, T., Vortex rings, in *Fluid Vortices*, editor S. Green, Kluwer Academic Press, 1995, 95–153.

[7] Maxworthy, T., The structure and stability of vortex rings, *Journal of Fluid Mechanics*, **51**, 1972, 15–32.

[8] Shariff, K. and Leonard, A., Vortex rings, *Annual Review of Fluid Mechanics*, **24**, 1992, 235–279.

[9] Westerweel, J. and Scarano, F., Universal outlier detection for piv data, *Experiments in Fluids*, **39**, 2005, 1096–1100.